

Modelling of Two-Phase Bubbly Flow over a Flat Plate

S. Vahaji¹, L. Chen², S.C.P. Cheung¹ and J.Y. Tu¹

¹ School of Aerospace, Mechanical and Manufacturing Engineering (SAMME)

RMIT University, Victoria 3083, Australia

² Maritime Division, Defence Science and Technology Organisation

Victoria 3032, Australia

Abstract

In two-phase flows, the flow behaviour is closely coupled with the interfacial momentum transfer of which is characterised by the bubble size distribution. In this regards, a two-phase bubbly flow over flat plate using an Eulerian-Eulerian two-fluid model coupled with the MUSIG (MUltiple Size Group) population balance model is numerically investigated and validated against experimental results for a range of flow conditions.

Different kernels of bubble break-up and coalescence mechanisms are selected to investigate their influence on the bubble size distribution. The turbulence is modeled based on Reynolds averaged Navier-Stokes (RANS) transport equations for carrier and dispersed phases, where Shear Stress Transport (SST) model is employed for the carrier. Zero equation turbulence is adopted for the dispersed phases. The skin friction coefficient validation, void fraction distribution and bubble size distribution for different bubble rates are investigated and discussed.

Introduction

Two-phase gas-liquid flows are prevalent in many industries such as nuclear, chemical, mineral, pharmaceutical, food, civil and metallurgy. Such flows have complex structures which can dynamically evolve in terms of the local hydrodynamic variables like bubble size distribution, bubble coalescence and breakage rate, void fraction and interfacial area concentration. Studying the bubble size distribution may also reveal more detail information like the investigation on the noise that is caused by bubble break-up in a process. Furthermore, the study of the mechanisms of drag reduction (DR) has been prevailing over the past few decades, both numerically and experimentally, in order to achieve a highly efficient ship tanker, submarine or even the transport of fluids to a long distance through pipelines. One theory in literature is that the drag reduction is caused by the density ratio effect which depends on the material properties of the continuous phase (water) and the dispersed phase (bubbles). Since the density ratio of the phases is high, the viscosity of the mixture is increased, and the turbulent momentum transfer caused by the dispersed phase is decreased. Consequently, the wall shear stress and the skin friction is reduced.

This theory was derived by the assumption of constant bubble size throughout the downstream of the boundary layer [7] which indicates the neglect of the evolution of bubble size distribution caused by the bubble break-up and coalescence mechanisms. The bubble size distribution has the direct and significant influence on the bubble dynamics whose ignorance may be only valid for the problems with a considerably low bubble number density. This assumption may cause considerable error to the numerical predictions especially for the cases with high number densities

where the coalescence and break-up mechanisms play an important role in bubble dynamics. Murai et al. [8] reported that intermediate/large bubbles were formed in the downstream region due to the high rate of bubble coalescence in the shear layer.

Mohanarangam et al. [6] numerically investigated the role of the micro-bubble in drag reduction. In this paper, the influence of bubble size distribution in drag reduction of slightly bigger bubbles is investigated. For this purpose, a two-fluid model along with a10 bubble classes MUSIG (Multi-SIze-Group) model is employed. The influence of different coalescence rates is studied through the application of different coalescence kernels in the population balance model. The skin friction ratios are compared against the experimental data of Madavan et al. [4]. The void fraction profiles along the outlet as well as the bubble size distribution for different gas injection rates are investigated.

Two-Fluid Model

The current numerical simulations are based on the two-fluid model approach. The Eulerian-Eulerian modelling framework is based on ensemble-averaged of mass, momentum and energy transport equations for each phase. Regarding the liquid phase (l) as continuum and the vapour phase (bubbles) as dispersed phase (g), these equations can be written as:

Continuity equation of liquid phase

$$\frac{\partial \rho_l \alpha_l}{\partial t} + \nabla \cdot (\rho_l \alpha_l \vec{u}_l) = \Gamma_{lg} \quad (1)$$

Continuity equation of vapour phase

$$\frac{\partial \rho_g \alpha_g f_i}{\partial t} + \nabla \cdot (\rho_g \alpha_g \vec{u}_g) = S_i - f_i \Gamma_{lg} \quad (2)$$

Momentum equation of liquid phase

$$\begin{aligned} \frac{\partial \rho_l \alpha_l \vec{u}_l}{\partial t} + \nabla \cdot (\rho_l \alpha_l \vec{u}_l \vec{u}_l) &= -\alpha_l \nabla P + \alpha_l \rho_l \vec{g} \\ &+ \nabla [\alpha_l \mu_l^e (\nabla \vec{u}_l + (\nabla \vec{u}_l)^T)] \\ &+ (\Gamma_{lg} \vec{u}_g - \Gamma_{gl} \vec{u}_l) + F_{lg} \end{aligned} \quad (3)$$

Momentum equation of vapour phase

$$\begin{aligned} \frac{\partial \rho_g \alpha_g \vec{u}_g}{\partial t} + \nabla \cdot (\rho_g \alpha_g \vec{u}_g \vec{u}_g) &= -\alpha_g \nabla P + \alpha_g \rho_g \vec{g} \\ &+ \nabla [\alpha_g \mu_g^e (\nabla \vec{u}_g + (\nabla \vec{u}_g)^T)] \\ &+ (\Gamma_{gl} \vec{u}_l - \Gamma_{lg} \vec{u}_g) + F_{gl} \end{aligned} \quad (4)$$

The interfacial force F_{lg} appearing in equation (3) is formulated through appropriate consideration of different sub-forces

affecting the interface between each phase. For the liquid phase, the interfacial force comprises the sum of the sub-forces such as drag, lift, wall lubrication and turbulent dispersion respectively. Note that for the gas phase, $F_{gl} = -F_{lg}$.

Interfacial transfer of momentum, heat and mass is directly dependent on the contact surface area between the two phases and is characterized by the interfacial area per unit volume between phase α and phase β , which is the interfacial area density $A_{\alpha\beta}$. The Particle Model is used to model this interfacial transfer between the two phases, assuming that one of the phases is continuous (phase α) and the other is dispersed (phase β). The surface area per unit volume is then calculated by assuming that phase β is present as spherical particles of mean diameter d_β . The interphase contact area after some modifications for robustness is given by

$$A_{\alpha\beta} = \frac{6r_\beta^*}{d_\beta} \quad (5)$$

where

$$r_\beta^* = \begin{cases} \max(r_\beta, r_{min}) & \text{if } (r_\beta < r_{max}) \\ \max\left(\frac{1-r_\beta}{1-r_{max}} r_{max}, r_{min}\right) & \text{if } (r_\beta > r_{max}) \end{cases} \quad (6)$$

The non-dimensional interphase transfer coefficients may be correlated in terms of the particle Reynolds number and is given by

$$Re_{\alpha\beta} = \frac{\rho_\alpha |U_\beta - U_\alpha| d_\beta}{\mu_\alpha} \quad (7)$$

where μ_α is the viscosity of the continuous phase α .

Population Balance Model

On the right hand side of equation (2), S_i represents the additional source terms due to coalescence and breakage for the range of bubble classes that can exist within the vapour phase. The Multi-Size-Group (MUSIG) population balance model has been adopted to account for the non-uniform bubble size distribution in subcooled boiling flows. The model divides the continuous size range of bubbles into a number of discrete classes and assumes each bubble class travel at the same mean algebraic velocity. Continuity equation for the individual number density of bubble class i can be expressed as follow [1]:

$$\frac{\partial n_i}{\partial t} + \nabla \cdot (\bar{u}_g n_i) = \left(\sum_j R_j \right)_i + (R_{ph})_i \quad (8)$$

where $(\sum_j R_j)_i$ represents the net change in the number density distribution due to coalescence and break-up processes. The term $(R_{ph})_i$ constitutes the essential formulation of the source/sink rate for the phase change processes associated with subcooled boiling flow. Detailed expressions of these rates can be found in [10].

Here, the break-up rate of bubbles of volume v_j into volume v_i is modelled according to the model developed by Luo and Svendsen [3]. The model is developed based on the assumption of bubble binary break-up under isotropic turbulence situation. The daughter size distribution has been taken account using a stochastic breakage volume fraction f_{BV} . Incorporate the increase coefficient of surface area $c_f = [f_{BV}^{2/3} + (1-f_{BV})^{2/3} - 1]$ into the breakage efficient, the break-up rate of bubbles can be obtained as:

$$\frac{\Omega(v_j; v_i)}{(1-\alpha_g)n_j} = C \left(\frac{\varepsilon}{d_j^2} \right)^{1/3} \int_{\xi_{min}}^1 \frac{(1+\xi)^2}{\xi^{11/3}} \times \exp \left(-\frac{12c_f\sigma}{\beta\rho_l\varepsilon^{2/3}d_j^{5/3}\xi^{11/3}} \right) d\xi \quad (9)$$

where $\xi = \lambda/d_j$ is the size ratio between an eddy and a particle in the inertial sub-range and consequently $\xi_{min} = \lambda_{min}/d_j$ and C and β are determined, respectively, from fundamental consideration of drops or bubbles breakage in turbulent dispersion systems to be 0.923 and 2.0.

On the other hand, bubble coalescence occurs via collision of two bubbles which may be caused by wake entrainment, random turbulence and buoyancy. However, only turbulence random collision is considered in the present study as all bubbles are assumed in spherical shape (wake entrainment becomes negligible). Furthermore, as all bubbles travel at the same velocity in the MUSIG model, buoyancy effect is also eliminated. The coalescence rate considering turbulent collision taken from Prince and Blanch [9] can be expressed as:

$$\chi_{ij} = \frac{\pi}{4} [d_i + d_j]^2 (u_{ti}^2 + u_{tj}^2)^{0.5} \exp \left(-\frac{t_{ij}}{\tau_{ij}} \right) \quad (10)$$

where τ_{ij} is the contact time for two bubbles given by $(d_{ij}/2)^{2/3}/\varepsilon^{1/3}$ and t_{ij} is the time required for two bubbles to coalesce having diameter d_i and d_j estimated to be $[(d_{ij}/2)^3 \rho_l/16\sigma]^{0.5} \ln(h_o/h_f)$. The equivalent diameter d_{ij} is calculated as: $d_{ij} = (2/d_i + 2/d_j)^{-1}$. According to Prince and Blanch [9], for air-water systems, experiments have determined the initial film thickness h_o and critical film thickness h_f at which rupture occurs to 1×10^{-4} and 1×10^{-8} m, respectively. The turbulent velocity u_t in the inertial sub-range of isotropic turbulence is given by: $u_t = \sqrt{2}\varepsilon^{1/3}d^{1/3}$.

Numerical Details

The conservation equations for mass, momentum and energy of each phase are discretised using the finite volume technique. A total number 10 bubble classes are prescribed for the dispersed phases. This represents an additional set of 10 transport equations of which are progressively solved and coupled with the flow equations during the simulations. Two sets of simulations with break-up coefficient of 1.0 and 0.05 are run in this study. Figure 1 shows the schematic diagram of the numerical model used in our computations. The numerical simulations are performed with a velocity inlet and a pressure outlet, on the left and right side of the 2D computational domain respectively. The top boundary is modelled as traction-free opening, wherein the height of the computational domain reflects half the height of the original test section. The bottom part of the domain has been divided into three distinct sections, section 1 & 3 were modelled as walls emulating the experimental boundary conditions, whereas the section 2 is modelled as the inlet boundary condition for our gas inlet imitating the experimental conditions of gas injection throughout the porous plate.

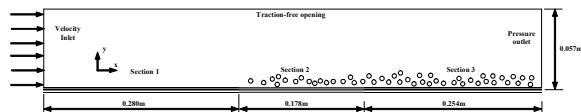


Figure 1. Schematic diagram of the numerical model.

A uniform liquid velocity is specified at the inlet of the test section and different gas flow rates are specified along the section 2 of the computational domain. The free stream velocities and the gas injection rates used in the simulations are

summarized in Table 1. An area permeability of 0.3 which lies in line with the sintered metal used in the experiments and also employed in the numerical work of Kunz et al. [2] is used all along section 2 for gas injection purposes. At the outlet, a relative averaged static pressure of zero is specified. For all flow conditions, reliable convergence are achieved within 2500 iterations when the RMS (root mean square) pressure residual dropped below 1.0×10^{-5} . A fixed physical time scale of 0.002s is adopted for all steady state simulations.

Case	Air flow rate Q_a (m^3/s)	Water free stream velocity (m/s)	Re_t based on the total plate length
Q0-V9.6(C_{f0})	0	9.6	7.66×10^6
Q1-V9.6	0.001	9.6	7.66×10^6
Q2-V9.6	0.0015	9.6	7.66×10^6
Q3-V9.6	0.002	9.6	7.66×10^6
Q4-V9.6	0.0025	9.6	7.66×10^6
Q5-V9.6	0.003	9.6	7.66×10^6

Table 1. Input boundary conditions for the computational model.

Results and Discussion

The two-phase bubbly flow is created by the injection of air through the ‘section 2’ of the computational domain. The depth of the domain is assumed to be 0.102 m, in order to calculate the gas inlet volumetric flow rates though the section. The gas injection rates (Q_a) have been varied through the section and their skin friction coefficients have been tabulated across. Figure 2 shows the comparison of our simulated skin friction ratios for both of the numerical simulations of break-up coefficients equal to 1.0 and 0.05 against the experimental findings of Merkle and Deutch [5] for varying gas injection rates (Q1-Q5). In this graph, C_f & C_{f0} are the skin-friction coefficients with and without the gas injection respectively. The skin-friction co-efficient throughout our numerical study have been obtained by averaging out the entire flat plate of ‘section 3’. It can be seen that both models show reasonable agreement with experiment which allows the further investigation of the flow.

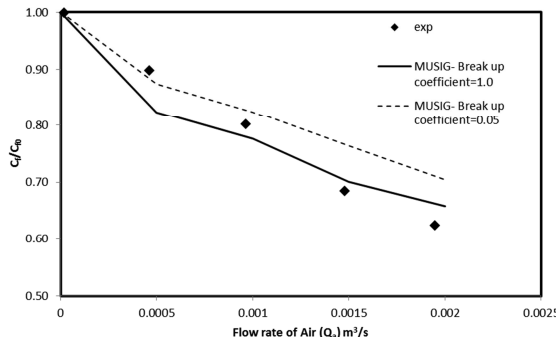


Figure 2. Comparison of computed skin-friction coefficient with experimental data of Merkle and Deutch [5].

Figure 3a presents the void fraction profiles for the dispersed phase for the free-stream velocity of 9.6 m/s with break-up coefficient of 0.05, along the outlet plane of the geometry. Figure 3b depicts similar graph for break-up coefficient of 1.0. In both graphs of Figure 3, y^+ is calculated from

$$y^+ = \frac{yu_\tau}{v} \quad (11)$$

where y is vertical distance from no-slip wall, u_τ is the friction velocity and v is the kinematic viscosity. It can be seen that there is a sharp increase in the void fraction for a y^+ value of about 400 for the maximum flow rate, with the maximum occurring at around 0.25, whereas from figure 3b, where break-up coefficient

is 1.0, it can be seen that the void fraction profiles for the dispersed phase occurring in a slightly different pattern with the maximum occurring at around 0.8 at a distance around $y^+ = 150$. This occurrence of maximum void fraction can be studied to explain the degree of drag reduction between the two break-up coefficients considered in our study. For the case ‘b’, where the maximum void fraction is higher than that of case ‘a’, a higher degree of drag reduction is seen. This is attributed to the fact that by having a lower break-up coefficient, bubbles may not break into smaller size, so they can rise and distribute themselves within the boundary layer easier.

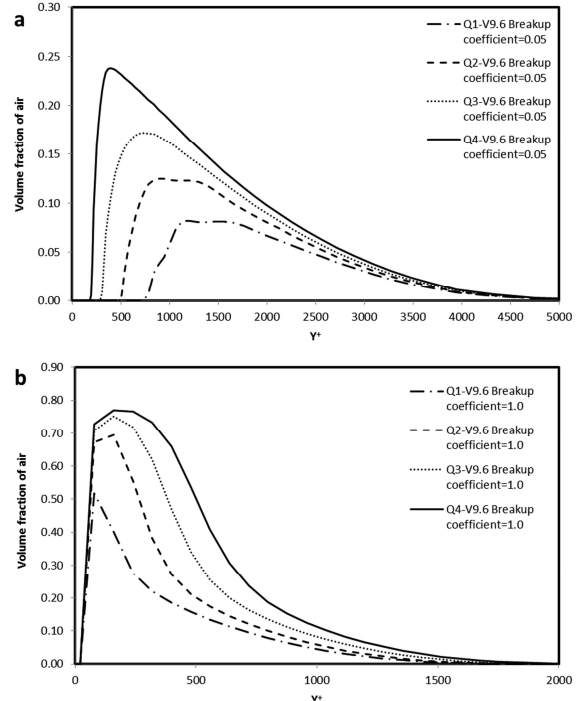


Figure 3. Volume fraction of air along the outlet for (a) break-up coefficient = 0.05, (b) break-up coefficient = 1.0.

This approves the findings that with smaller bubbles, higher drag reduction could be achieved. It can be seen that for all the cases by increasing the gas flow rate, the void fraction of the injected air increases and later due to the dispersion and also the washing down effect of the continuous phase flattens out. It is interesting to point out that there is a thin film of liquid which regardless of the gas injected flow rates covers all over the wall. By the comparison of Figures 3a and b, it can be concluded that as the liquid film becomes thinner, the shear stress of the film decreases. Consequently, the skin friction ratio C_f/C_{f0} becomes lower, and drag reduction becomes higher. Also, this finding is in accordance with the fact that with the increase in the gas flow rate, the skin friction ratio decreases due to subsequent thinning of the liquid film adjacent to the wall. In the numerical simulations, the influence of bubble coalescence and break-up is investigated through the application of different coalescence kernels and the break-up coefficient. Figure 4 depicts the bubble size distribution predictions at the outlet for different coalescence kernels of Prince & Blanch, Coulaloglou & Tavlarides, and Lehr et al. for (a) case Q1-V9.6 and (b) case Q3-V9.6 with the break-up coefficient of 0.05. In figure 5, all the numerical set up is kept unchanged except the break-up coefficient to investigate the influence of break-up mechanism. By comparing figures 4 and 5, it is noticeable that figure 4 predicts larger bubbles. The reason is that break-up coefficient is considered to be 20 times less which

prevents the efficient breakage mechanism of the bubbles. As a result, larger bubbles exist throughout the outlet.

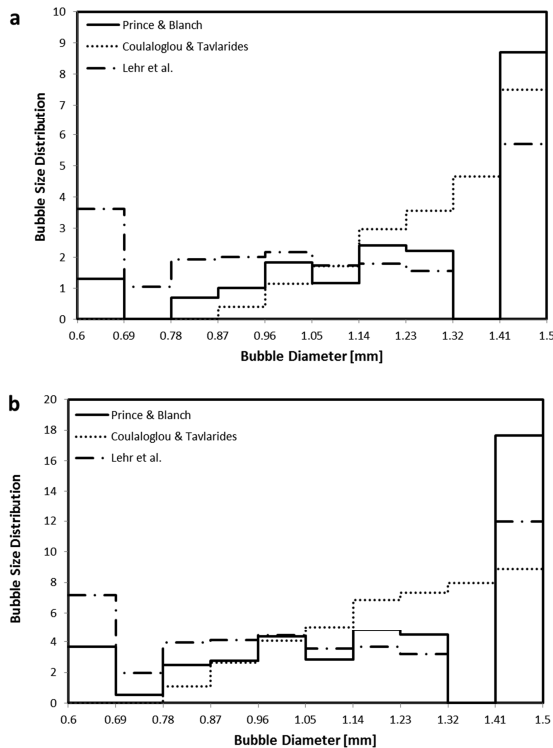


Figure 4. Bubble diameter distribution function with break-up coefficient = 0.05 for (a) Q1-V9.6 and (b) Q3-V9.6.

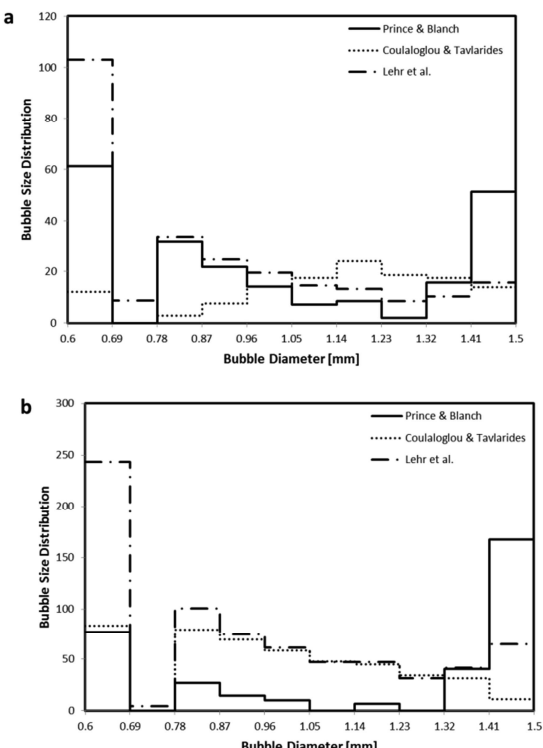


Figure 5. Bubble diameter distribution function with break-up coefficient = 1.0 for (a) Q1-V9.6 and (b) Q3-V9.6.

These predictions are in accordance with the numerical predictions of Mohanarangam et al. [6] where the distribution tends to have a peak at larger class in lower break-up coefficient. Also, in both figures case Q3-V9.6 yields in higher volume fraction predictions which confirms the higher injection rate of the gas in the domain. The kernel of Coualaloglu & Tavlarides predicts differently in figures 4 and 5. This kernel predicts an almost constant increase in bubble size in each bubble class in Figure 4; whereas, in figure 5, it predicts an almost constant decrease. Both Prince & Blanch and Lehr et al. kernels tend to predict a bimodal bubble size distribution in almost all cases with a difference that the peak for smaller size is higher in figure 5. By having a closer examination, one could see that Prince & Blanch predicts larger bubbles which indicates a higher rate of coalescence compared to other kernels. However, the question of which kernel is predicting better for the given flow condition, could only be answered by having experimental data of bubble size distribution which could validate the numerical predictions.

Conclusions

Numerical simulation of two-phase bubbly flow over flat plate has been successfully investigated using MUSIG model with different coalescence and break-up kernels. The numerical predictions of skin friction for both break-up conditions show good agreement with experimental results. Different coalescence kernels show different behaviours in prediction of bubble size distribution which ascertains the importance of such mechanisms in bubble dynamics. However, further study is directed towards investigating the accuracy of such mechanisms.

Acknowledgments

The authors acknowledge and appreciate the financial support by DSTO (Defence Science and Technology Organisation).

References

- [1] Kumar, S.&Ramkrishna, D., On the solution of population balance equations by discretization—I. A fixed pivot technique. *Chemical Engineering Science*, **51**(8), 1996, 1311-1332.
- [2] Kunz, R.F., Deutsch, S.&Lindau, J.W. Two fluid modeling of microbubble turbulent drag reduction. in *ASME/JSME 2003 4th Joint Fluids Summer Engineering Conference*. 2003. American Society of Mechanical Engineers.
- [3] Luo, H.&Svendsen, H.F., Theoretical model for drop and bubble breakup in turbulent dispersions. *AIChE Journal*, **42**(5), 1996, 1225-1233.
- [4] Madavan, N.K., Deutsch, S.&Merkle, C.L., Reduction of turbulent skin friction by microbubbles. *Physics of Fluids*, **27**(2), 1984, 356-363.
- [5] Merkle, C.L.&Deutsch, S., Microbubble Drag Reduction in Liquid Turbulent Boundary Layers. *Applied Mechanics Reviews*, **45**(3), 1992, 103-127.
- [6] Mohanarangam, K., Cheung, S.C.P., Tu, J.Y.&Chen, L., Numerical simulation of micro-bubble drag reduction using population balance model. *Ocean Engineering*, **36**(11), 2009, 863-872.
- [7] Moriguchi, Y.&Kato, H., Influence of microbubble diameter and distribution on frictional resistance reduction. *Journal of marine science and technology*, **7**(2), 2002, 79-85.
- [8] Murai, Y., Fukuda, H., Oishi, Y., Kodama, Y.&Yamamoto, F., Skin friction reduction by large air bubbles in a horizontal channel flow. *International journal of multiphase flow*, **33**(2), 2007, 147-163.
- [9] Prince, M.J.&Blanch, H.W., Bubble coalescence and break-up in air-sparged bubble columns. *Aiche Journal*, **36**(10), 1990, 1485-1499.
- [10] Yeoh, G.H.&Tu, J.Y., Thermal-hydrodynamic modeling of bubbly flows with heat and mass transfer. *Aiche Journal*, **51**(1), 2005, 8-27